Energy Engineering

Tech Science Press

https://doi.org/10.32604/ee.2026.076849

ARTICLE

Numerical Investigation of Proppant Transport Heterogeneity in Multi-Cluster Horizontal Well Fracturing: A Computational Fluid Dynamics Study

Yixuan Wang[1], Yanchao Li[1], Qiang Feng[1], Haicheng Sun[2], Guchang Zhang[3], Zhiming Zhao[1], Jianfeng Xiao[1], Jingyun Huang[1] and Tiankui Guo[3,*]

[1]Shale Gas E&D Project Department, CNPC Chuanqing Drilling Engineering Co., Ltd., Chengdu, China
[2]Petroleum Engineering Technology Research Institute, Shengli Oilfield Company, SINOPEC, Dongying, China
[3]School of Petroleum Engineering, China University of Petroleum (East China), Qingdao, China

*Corresponding Author: Tiankui Guo. Email: guotiankui@126.com

Received: 27 November 2025; Accepted: 15 January 2026; Published: 12 November 2026

ABSTRACT: Achieving uniform proppant distribution among multiple perforation clusters is essential for the effectiveness of horizontal well fracturing, yet remains challenging due to complex solid-liquid transport mechanisms. This study presents a comprehensive numerical investigation using Computational Fluid Dynamics to analyze proppant transport heterogeneity in a full-scale 90-m horizontal wellbore with five perforation clusters. An Eulerian-Eulerian multiphase model is employed to simulate proppant transport and settling in the wellbore and perforations. The effects of key operational and geometric parameters—including injection rate, proppant concentration and size, fluid viscosity and phase angle—are systematically evaluated. Results demonstrate that flow rate and fluid viscosity dominate proppant inertial and settling behavior: higher rates enhance axial transport but exacerbate uneven distribution toward the toe, while increased viscosity significantly improves suspension and entry efficiency into distal clusters. Proppant size directly influences settling dynamics, with finer particles exhibiting superior uniformity. Furthermore, the phase angle of perforations considerably affects transport uniformity, with a 45° spiral configuration effectively mitigating bottom-side entry bias and improving circumferential proppant distribution. The findings provide critical insights into the interplay of inertial, viscous and gravitational forces governing proppant placement, offering a validated numerical basis for optimizing perforation design and pumping parameters to achieve more uniform stimulation in unconventional reservoirs.

KEYWORDS: Proppant transport; horizontal well fracturing; multi-cluster perforation; CFD simulation; uniform distribution; parameter optimization

1 Introduction

Horizontal staged multi-cluster fracturing technology is a key method for enhancing the development efficiency of unconventional oil and gas reservoirs [1–3]. This technique involves injecting high-pressure fluid into the reservoir to create a complex multi-branch fracture network, thereby significantly expanding the hydrocarbon seepage area [4–6]. During the fracturing process, proppant plays a critical role [7]. Its primary function is to keep the fractures open through physical support after fracturing, forming stable channels with high conductivity and ensuring efficient hydrocarbon flow into the wellbore [8–10]. In recent years, with continued in-depth research, the understanding of proppant transport behavior has progressively evolved from macroscopic placement within fractures to the dynamic transport process along the entire wellbore–fracture path [11,12]. Although the final distribution of proppant in the fractures directly determines their

Copyright © 2027 The Authors. Published by Tech Science Press. This work is licensed under a Creative Commons Attribution 4.0 International License, which permits unrestricted use, distribution, and reproduction in any medium, provided the original work is properly cited.

conductivity and the effectiveness of the fracturing treatment, the transport of proppant in the wellbore and perforations—as the prerequisite and foundation for its entry into the fractures—is equally crucial. It fundamentally influences the uniform entry and effective support of proppant in each cluster [13,14]. A comprehensive understanding and precise control of the dynamic behavior of proppant in the wellbore and perforations are essential to solving the challenges of uniform fracture initiation and balanced proppant distribution among clusters, ultimately serving as a critical pathway toward the efficient development of unconventional oil and gas resources.

The spatial distribution of proppant within the wellbore serves as a critical determinant for the effectiveness of multi-cluster staged fracturing in horizontal wells. The uniformity of this distribution directly influences the degree of proppant coverage achieved in individual fracture clusters, thereby governing the overall efficiency of reservoir stimulation. In a comparative study, Shah and Lord experimentally evaluated the proppant-carrying capacities of linear/crosslinked gels and water-based fluids using a horizontal flow loop apparatus [15]. They introduced critical settling velocity (the flow rate at which particles begin to deposit) and resuspension velocity (the minimum velocity required to re-entrain deposited particles) as key evaluation parameters and found that the critical velocity for non-Newtonian fracturing fluids is significantly lower than that for Newtonian fluids. Arnipally further investigated the influence of particle size on critical velocity using horizontal flow tests [16]. The results indicated a strong positive correlation between the critical resuspension velocity of sandbed particles and their diameter—a phenomenon attributed to the scaling effects of gravitational force and interparticle friction. Xing et al. revealed non-monotonic transport behavior of medium and large proppant particles in horizontal pipe flow [17]. Their study demonstrated that the critical resuspension velocity initially increases and then decreases with increasing proppant concentration. When the volumetric concentration exceeds a critical threshold of 7%, the critical velocity stabilizes at around 3.5 $m \cdot s^{-1}$ before gradually declining. Proppant settling in the wellbore significantly affects its transport into perforations. Along the wellbore axis, proppant flow velocity decreases while concentration increases. Settling begins once the local velocity falls below the critical value. Field observations show that proppant tends to settle predominantly near the toe-end clusters. As the sand dune grows, the flow area constricts, which increases the fluid velocity above the critical level and eventually leads to a dynamic equilibrium. Nevertheless, proppant settling still occurs in field operations even under high pump rates. Ngameni et al. conducted experimental studies using a 30-ft horizontal wellbore equipped with three perforation clusters [18]. Their work confirmed that all types of proppant experience significant retention in the wellbore, even when the flow rate exceeds the theoretical critical velocity. Ahmad and Miskimins performed experiments on a physical model of a horizontal wellbore with three perforation clusters and identified key mechanisms governing proppant transport [19]. Their data suggested that under low flow rates, high-density proppant settles preferentially due to a notable decrease in the ratio of vertical settling velocity to horizontal flow velocity. Using computational fluid dynamics (CFD), Sinkov et al. identified a pronounced proppant concentration polarization effect near the wellbore wall [20]. Their simulations indicated that high shear flow near heel-side perforations suppresses particle transport and reduces perforation capture efficiency, while the low-velocity swirling environment around toe-side perforations tends to induce proppant phase separation. Aijaz and Sharma employed CFD simulations to investigate proppant settling behavior and its impact on perforation efficiency [21]. Their mechanistic analysis revealed that the last cluster at the toe end becomes a preferential settling zone due to flow velocity attenuation. The resulting sand bed reduces the flow area, which in turn increases the velocity until it surpasses the critical resuspension velocity. Although the total amount of settled proppant in the wellbore is limited, the induced micro-scale fluid–solid coupling effects significantly alter the flow behavior and pressure distribution within the wellbore. While the aforementioned studies have qualitatively elucidated the general principles of proppant settling, they have not yet established a numerical

model that can be reliably scaled to field conditions. Moreover, the actual settling dynamics of proppant in horizontal well sections remain insufficiently explored, highlighting the need for further investigation into proppant settling behavior under various operational conditions.

Uniform proppant distribution among perforation clusters is ideal for ensuring effective fracture support. However, field data indicate that certain clusters contribute little to production, revealing significant proppant distribution heterogeneity [22]. Crespo et al. identified an "80/20 rule" in shale reservoir productivity, where 70% of production comes from only 30% of effective perforation stages [23]. This highlights the importance of precise proppant transport control between clusters to enhance reservoir stimulation efficiency. Optimizing proppant spatial distribution can fully unlock the production potential of unconventional reservoirs, providing theoretical support for economic development. Extensive experimental and numerical studies have been conducted on inter-cluster proppant allocation. Experiments often use visualized wellbore setups to monitor perforation flow and collect proppant, while numerical simulations primarily employ CFD-DEM and CFD methods [24]. Ahmad and Miskimins, through a 90-m horizontal well experiment, found that larger and denser proppants exhibit poorer distribution uniformity, whereas lightweight ceramic proppants significantly improve it [25]. Zhang et al., using CFD-DEM simulations, revealed nonlinear effects of wellbore inclination on proppant transport in differently oriented perforations [26]. Li et al., in a 1.5-m visualized experiment, identified a critical injection condition in slickwater systems that achieves a dynamic balance between proppant settling and transport, enhancing distribution uniformity [27]. They also noted a threshold effect of proppant concentration, where higher concentrations improve transport efficiency but increase screen-out risk. Bahri et al., via a 9.14-m wellbore experiment, demonstrated that optimizing the perforation angle to 70° enhances swirl flow, improving lateral transport and near-wellbore distribution uniformity [28]. Liu et al. revealed a pronounced bias in proppant entry, with bottom perforations capturing significantly more proppant than top ones—a disparity attributed to gravitational settling and particle inertia that was particularly pronounced in toe-side clusters [29]. Sinkov et al. further emphasized proppant inertia as the main cause of uneven distribution. As flow rate decreases along the wellbore, proppant in the toe region settles and accumulates at the bottom, significantly reducing its transport velocity [30]. In summary, existing experimental setups vary greatly in scale (1.5–90 m) and often use simplified models, limiting their ability to represent full-wellbore multi-cluster competitive flow and leading to challenges in scalability and applicability. Furthermore, while previous studies have examined individual parameters in isolation, there remains a lack of comprehensive, coupled analysis of how operational parameters (injection rate, proppant concentration), fluid properties (viscosity), and geometric factors (perforation phase angle, wellbore inclination) interact to affect proppant distribution in full-scale multi-cluster systems. This study addresses this gap by providing a systematic investigation of these coupled effects using a validated CFD model that captures the complete transport pathway from wellbore entry to fracture entry.

Addressing the current research gaps in proppant transport regarding experimental scale, multi-factor coupling and full-path analysis, this study employs Computational Fluid Dynamics (CFD) to establish a full-scale 90-m horizontal wellbore model with five perforation clusters, consistent with field operational conditions. The numerical simulation systematically replicates the entire proppant transport process from the pump injection inlet until entry into the fractures. It focuses on investigating the coupled effects of multiple factors, including proppant particle size, sand ratio, fracturing fluid properties, injection rate and wellbore and perforation geometric parameters. The study aims to elucidate the underlying mechanisms of uneven proppant distribution among clusters and achieve quantitative analysis of proppant velocity and concentration at various locations. This research provides a numerical basis for establishing an accurate theory of uniform inter-cluster proppant placement and offers crucial technical support for optimizing perforation design and operational parameters to enhance reservoir stimulation effectiveness.

2 Methodology

The Eulerian multiphase flow model is employed to simulate proppant transport within the wellbore and among perforation clusters. This approach treats both the proppant and the fracturing fluid as interpenetrating continua, with its key advantage lying in the detailed characterization of complex multiphase flow behavior. By establishing separate momentum equations for each phase, it accurately captures the strong interphase coupling effects [31]. As a computational fluid dynamics (CFD) method, the Eulerian multiphase approach significantly reduces computational time compared to coupled CFD-DEM (discrete element method) approaches [32,33]. The Eulerian-Eulerian model implementation is based on Kinetic Theory of Granular Flow, where particle-phase stresses are modeled through granular temperature representing velocity fluctuations. Key assumptions include: the Lun et al. viscosity model for solid-phase rheology, Syamlal-O'Brien drag law for interphase momentum exchange and a particle restitution coefficient of 0.9. This continuum approach was selected over CFD-DEM due to its computational feasibility for full-scale wellbore simulation, providing sufficient accuracy for capturing system-scale transport phenomena while maintaining practical computational costs.

2.1 Governing Equations for Two-Phase Flow

For multiphysics modeling of solid-liquid transport in wellbores, the Eulerian method treats dispersed particles as a continuum pseudo-fluid, enabling a unified field description. Its key advance is formulating independent conservation equations for the liquid and particle phases. Mass transport is constrained by an extended continuity equation and momentum coupling is captured via augmented Navier-Stokes equations with interphase source terms. A coupled multi-field strategy simultaneously solves for the spatiotemporal evolution of flow dynamics, pressure distribution and particle transport.

The continuity equation for either the solid or fluid phase is given by Eqs. (1) and (2):

$$\frac{\partial\left(\alpha_f\rho_f\right)}{\partial t}+\nabla\cdot\left(\alpha_f\rho_f v_f\right)=0 \tag{1}$$

$$\frac{\partial\left(\alpha_s\rho_s\right)}{\partial t}+\nabla\cdot\left(\alpha_s\rho_s v_s\right)=0 \tag{2}$$

where α_f is the fluid phase volume fraction (dimensionless), α_s is the solid phase volume fraction (dimensionless), ρ_f is the fluid density (kg/m^3), ρ_s is the solid density (kg/m^3), v_f is the fluid velocity vector (m/s), v_s is the solid velocity vector (m/s) and t is time (s).

The momentum equations for the fluid and solid phases are formulated as follows:

$$\frac{\partial}{\partial t}\left(\alpha_f\rho_f v_f\right)+\nabla\cdot\left(\alpha_f\rho_f v_f v_f\right)=-\alpha_f\nabla p_f+\nabla\cdot\tau_f+\alpha_f\rho_f g+\beta\left(v_s-v_f\right) \tag{3}$$

$$\frac{\partial}{\partial t}\left(\alpha_s\rho_s v_s\right)+\nabla\cdot\left(\alpha_s\rho_s v_s v_s\right)=-\alpha_s\nabla p_s+\nabla\cdot\tau_s+\alpha_s\rho_s g+\beta\left(v_f-v_s\right) \tag{4}$$

where p_s and p_f represents the pressure of solid phase and liquid phase, respectively (Pa), τ_s and τ_f represents the shear stress tensor of the solid phase and liquid phase, respectively (Pa), g representsthe acceleration due to gravity (m/s^2), β represents the inter-phase momentum exchange coefficient (kg·m^{-3}·s^{-1}).

2.2 Turbulence Model

During the continuous pumping of fracturing fluid into an extended-reach horizontal wellbore, proppant undergoes heterogeneous settling in the near-wellbore region, forming localized flow resistance barriers and resulting in heterogeneous transport behavior within the multiphase flow channels. This deposition

process not only diminishes the particle-carrying capacity of the slurry toward the toe-side fracture clusters but also induces significant alterations in the near-wall flow regime. The dynamic evolution of turbulent fluctuating energy in the flow system can be quantified by the turbulent fluctuation intensity parameter, as given in Eqs. (5) and (6):

$$I = \frac{u}{\overline{u}} = 0.16\,(\mathrm{Re})^{-1/8} \tag{5}$$

$$Re = \frac{\rho_f U L}{\mu_f} \tag{6}$$

where U represents the average fluid velocity across the section (m/s) and L denotes the diameter of the circular pipe (m).

Solid-liquid turbulent coupling is characterized by a pronounced two-way momentum and energy exchange between the proppant and fracturing fluid. Unsteady direct numerical simulation is best suited for resolving low-Reynolds-number flows in geometrically simple configurations. For broader CFD applications, however, the standard k-ε turbulence closure model is often employed. By solving the transport equations for turbulent kinetic energy (k) and its dissipation rate (ε), this model provides an effective compromise between computational expense and engineering accuracy, rendering it widely useful in routine industrial flow analysis. The standard k-ε model was selected for its proven robustness and computational efficiency in simulating high-Reynolds-number wellbore flows. It adequately captures the turbulent mixing governing large-scale slurry transport, which is the primary focus of this study. While advanced RANS models (e.g., RNG k-ε) may improve accuracy for specific features like strong curvature or swirl, the key mechanisms examined—axial velocity decay, gravitational settling and inertial perforation entry—are dominated by mean flow and interphase momentum effects, for which the standard model is sufficient. Future studies targeting microscale particle-turbulence interactions may benefit from comparing alternative closures.

The governing equations for the turbulent kinetic energy (k) and its dissipation rate (ε) are presented below [34]:

$$\frac{\partial}{\partial t}(\rho k) + \frac{\partial}{\partial x_i}(\rho k u_i) = \frac{\partial}{\partial x_j}\left[\left(\mu + \frac{\mu}{\sigma k}\right)\frac{\partial k}{\partial x_j}\right] + G_k - \rho\varepsilon \tag{7}$$

$$\frac{\partial}{\partial t}(\rho \varepsilon) + \frac{\partial}{\partial x_i}(\rho \varepsilon u_i) = \frac{\partial}{\partial x_j}\left[\left(\mu + \frac{\mu_t}{\sigma \varepsilon}\right)\frac{\partial \varepsilon}{\partial x_j}\right] + G_{1\varepsilon}\frac{\varepsilon}{k}G_k - C_{2\varepsilon}\rho\frac{\varepsilon^2}{k} \tag{8}$$

where k is the turbulent kinetic energy (m^2/s^2), ε is the turbulent dissipation rate (m^2/s^3), σ_k and σ_ε are the turbulent Prandtl numbers for k and ε, respectively, $C_{1\varepsilon}$ and $C_{2\varepsilon}$ are empirical constants, with values of 1.44 and 1.92, respectively. G_k and G_b represent the generation of turbulent kinetic energy due to mean velocity gradients and buoyancy ($kg/(m{\cdot}s^3)$), μ is the dynamic viscosity of the fluid (Pa·s) and μ_t is the turbulent eddy viscosity (Pa·s).

The critical settling velocity V_c of proppant in the wellbore is determined by the formula proposed by Ali Kökpınar and Göğüş [35]:

$$\frac{V_c}{\sqrt{gD}} = 0.055\left(\frac{d_s}{D}\right)^{-0.60} C_v^{0.27}\,(s-1)^{0.07}\left(\frac{\rho_f w_m d_s}{\mu_f}\right)^{0.30} \tag{9}$$

where V_c represents the critical flow velocity of the solid-liquid mixture ($m{\cdot}s^{-1}$); g denotes gravitational acceleration ($m{\cdot}s^{-2}$); D is the wellbore diameter (m); d_s stands for solid particle diameter (m); C_v indicates the volumetric concentration of solids (dimensionless); s refers to specific gravity (dimensionless); ρ_f is the fluid

density (kg·m^{-3}); w_m represents the particle settling velocity in the mixture (m·s^{-1}); and μ_f is the dynamic viscosity of the fluid (Pa·s).

The settling velocity, $w_{m,}$ of solid particles in a mixture of a given concentration can be expressed in terms of the settling velocity w of the same particles in clear water.

$$\frac{w_m}{w} = \frac{2-2C_v}{2-3C_v}\left(\frac{\sqrt{25+1.2\left(d_*'\right)^2}-5}{\sqrt{25+1.2d_*^2}-5}\right)^{1.5} \tag{10}$$

where w denotes the settling velocity of particles in clear water (m·s^{-1}); d_* represents the dimensionless particle diameter in clear water; and d_*' refers to the dimensionless particle diameter in the slurry mixture.

The settling velocity w of proppant in clear water and the kinematic viscosity v' of the slurry mixture are given by the following expressions:

$$\frac{wd_s}{v} = \left(\sqrt{25+1.2d_*^2}-5\right)^{1.5} \tag{11}$$

$$v' = \frac{2v}{2-3C_v} \tag{12}$$

where v represents the kinematic viscosity of clear water (m^2·s^{-1}) and v' denotes the kinematic viscosity of the slurry mixture (m^2·s^{-1}).

3 Model Establishment and Verification

3.1 Model Establishment

In current completion operations, the plug-and-perf technique is widely employed to isolate horizontal well sections. The number of perforation clusters and the number of perforations per cluster are determined based on the planned injection rate and the desired flow rate per perforation. According to industry practice, the flow rate per perforation typically ranges from 56 to 75 m/s. The total number of perforations is calculated from the ratio of the total injection rate to the target flow rate per perforation. It is recommended that the length of each perforation cluster be limited to less than twice the wellbore diameter to prevent the initiation of multiple competing fractures [36].

A numerical simulation model of a 90-m horizontal wellbore with a diameter of 139.7 mm was established, incorporating perforation clusters each 280 mm in length (Fig. 1). The cluster spacing was determined based on microseismic studies in the Barnett Shale, where the optimal spacing was found to be 1.5 times the fracture height. In the Eagle Ford formation, the recommended cluster spacing ranges from 10.7 to 12.2 m [37]; in this study, a spacing of 15 m was selected. According to laboratory tests, the perforation diameter should be 8–10 times larger than the average proppant diameter and was accordingly set to 9.5 mm [38]. To investigate proppant distribution in perforations at different orientations, a spiral perforation pattern with a phase angle of 45° was adopted. Each cluster contains 8 perforations with a depth of 100 mm and a diameter of 9.5 mm.

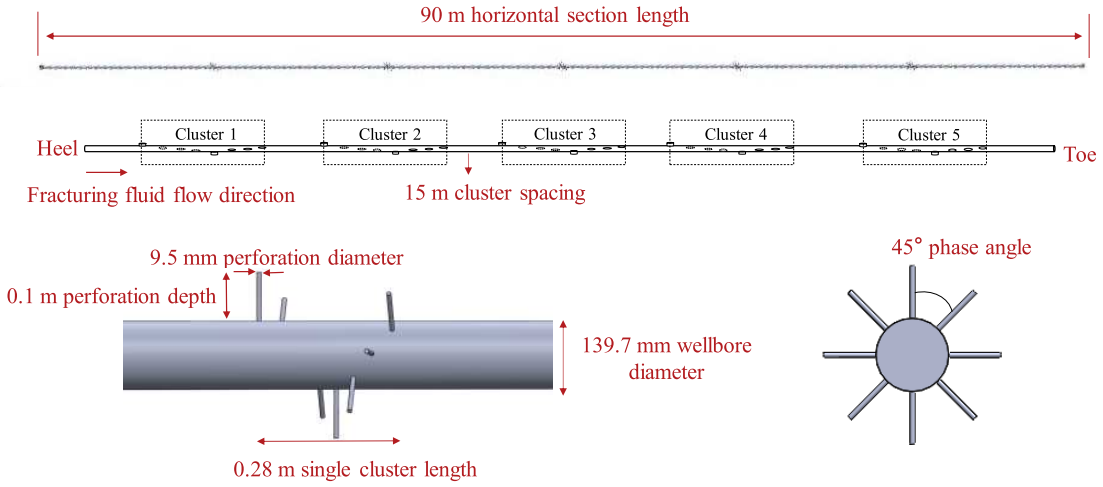


Figure 1: Numerical model of multi-cluster perforated wellbore dimensions.

To enhance computational efficiency, a local grid refinement approach was applied to the wellbore model, as illustrated in Fig. 2. Hexahedral structured meshes were employed in the perforation regions to ensure accuracy in simulating proppant entry from the wellbore into the perforations and to facilitate clear observation of flow characteristics. In areas with significant variations in flow velocity and pressure, grid refinement was implemented to ensure that the mesh around the perforations met the standards of a high-quality, fine-resolution grid. In non-perforated sections, the grid size was increased to effectively improve computational efficiency. While the local grid refinement strategy enables accurate resolution of perforation flow characteristics, the computational cost of simulating the full 90-m wellbore necessitated trade-offs in temporal resolution and required the use of a continuum-based Eulerian approach rather than more computationally intensive particle-tracking methods.

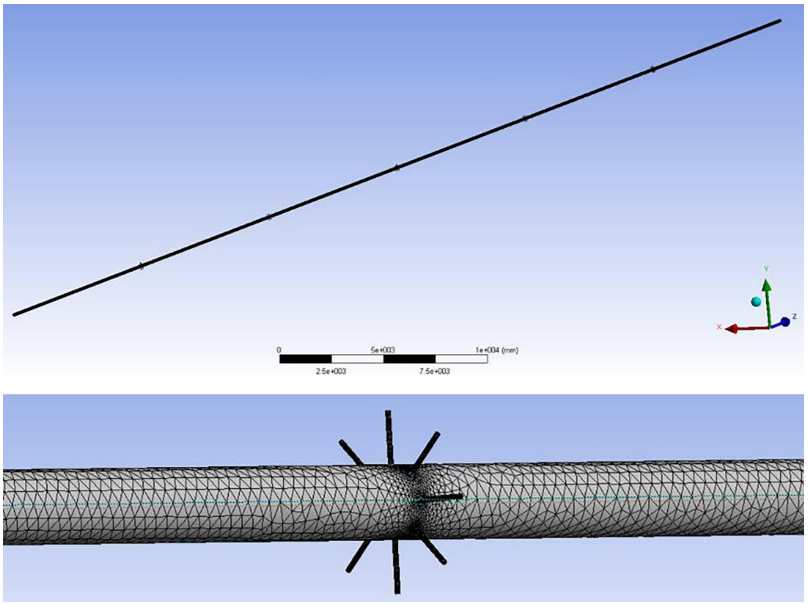


Figure 2: Mesh generation and local grid refinement.

A mesh sensitivity analysis was conducted to ensure numerical accuracy and solution independence. Three mesh resolutions were tested: coarse (≈1.8 million cells), medium (≈3.5 million cells) and fine (≈5.8 million cells). The results demonstrated excellent convergence, with differences in key parameters between medium and fine grids being minimal. Specifically, the pressure drop along the first 20 m of wellbore varied by less than 1.5%, while the proppant volume fraction at the fifth cluster outlet showed less than 2% variation. This confirms that the medium grid resolution provides sufficient accuracy while maintaining computational efficiency.

The transport and placement of proppant in the wellbore and through perforations were investigated by establishing a series of monitoring planes along the 90-m wellbore (Fig. 3). Circular planes perpendicular to the wellbore axis were placed at 5-m intervals to monitor the average volume fraction and flow velocity over each cross-section. Additional circular planes were positioned at the midpoints of each perforation tunnel, as well as at each perforation outlet, to similarly record the average volume fraction and velocity. Key evaluation parameters included the average flow velocity, volume fraction and pressure at the wellbore cross-sections, together with the average velocity and volume fraction at the perforation cross-sections.

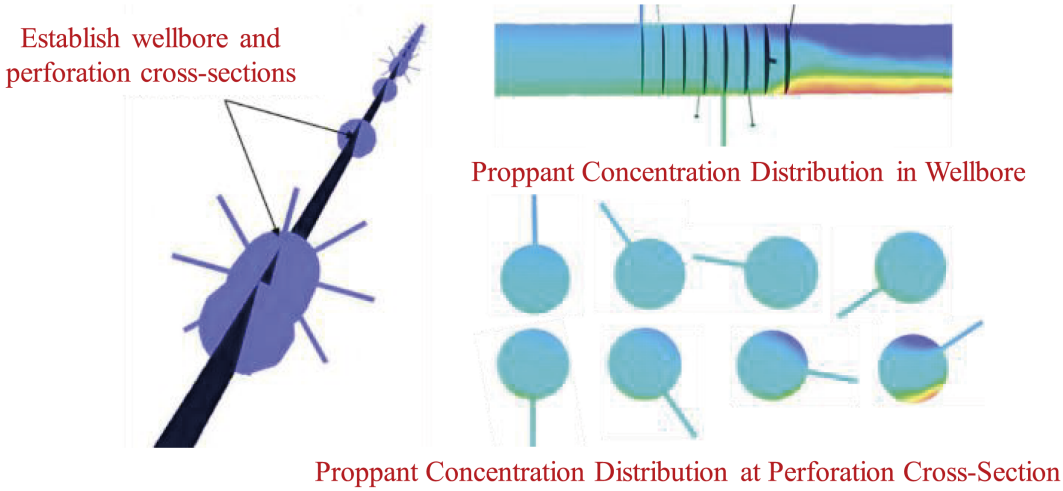


Figure 3: Establishment of the monitoring plane and presentation of simulation results.

The monitoring planes established at regular intervals and critical locations (Fig. 3) enabled quantitative assessment of proppant transport parameters. Area-weighted averaging was applied across each planar surface to compute representative values of flow velocity and proppant volume fraction, ensuring proper accounting of cross-sectional gradients. Data extraction was performed at flow equilibrium, with values averaged over a sufficient time period to establish stable means. This approach provided consistent methodology for comparing transport behavior at various wellbore positions and perforation locations.

3.2 Model Validation

Since this study focuses on the proppant distribution among multiple-cluster perforations, the numerical model developed was validated against the simulation results reported by Wang to verify its accuracy and precision [39]. A corresponding CFD model with a 60° phase angle was established and simulations were performed using the parameters listed in Table 1, which are consistent with those in the reference.

Table 1: Simulation parameter table of model validation.

Parameters	Value
Number of Clusters	5
Cluster Spacing (m)	13.7
Perforation Phase Angle (°)	60
Number of Perforations per Cluster	6
Casing Diameter (mm)	10.7
Wellbore Inner Diameter (m)	0.11
Pump Rate (m^3/min)	12.7
Proppant Concentration (%)	3.6
Fluid Viscosity (mPa·s)	2
Proppant Diameter (μm)	150
Perforation Diameter (mm)	6.35
Proppant Density (g/cm^3)	2.65

The proppant distribution ratios across different perforation clusters are compared in Fig. 4. The maximum discrepancy between the results from the present CFD model and the prior simulations by Wang is within 5%, which serves to validate the accuracy and precision of the model developed in this study.

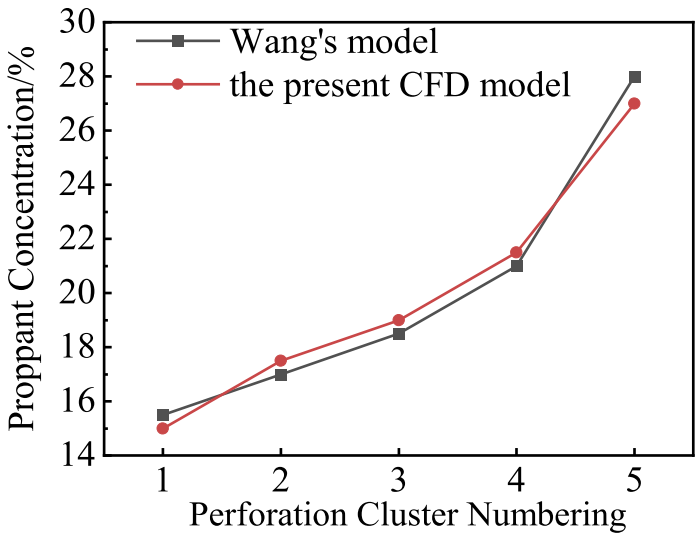


Figure 4: Comparison of proppant distribution proportions in perforation clusters.

4 Simulation Scheme

A total of 46 simulation cases were designed to systematically evaluate the effects of eight key parameters—flow rate, proppant concentration, fluid viscosity, proppant size, perforation diameter, wellbore inclination, cluster number and phase angle—on the transport and placement behavior of both fracturing fluid and proppant within the wellbore and perforation clusters. The baseline configuration adopted a flow velocity of 10 m/s, a proppant concentration of 10%, a proppant density of 2650 kg/m^3, a fluid viscosity of 5 mPa·s, a perforation diameter of 9.5 mm, five perforation clusters and a phase angle of 45° (corresponding to 8 perforations per cluster), with uniform outlet pressure maintained across all clusters. Additional

parameter combinations are summarized in Table 2. It is noted that the proppant sizes, derived from mean particle diameters, were assigned as follows: 0.633 mm for 20/40 mesh, 0.493 mm for 30/50 mesh, 0.311 mm for 40/70 mesh, 0.155 mm for 70/140 mesh, 0.074 mm for 200 mesh and 0.044 mm for 300 mesh.

Table 2: Simulation design parameters.

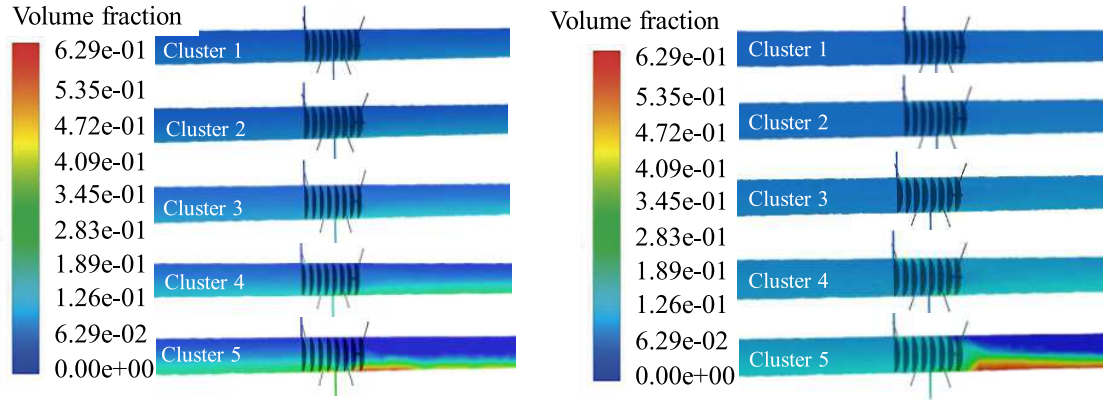
Parameters	Value
Flow Rate (m^3/s)	4/6/8/10/13/15/18
Proppant Concentration (%)	5/10/15/20/25/30/35
Fluid Viscosity (mPa·s)	1/5/10/15/20/25/30
Proppant Diameter (μm)	0.633/0.311/0.155/0.074/0.044/0.493
Perforation Diameter (mm)	9.5/11.5/13.5/15.5/17.5
Wellbore Inclination (°)	0/10/20/30/40/−10/−20/−30/−40
Number of Clusters	3/4/5/6
Phase Angle (°)	45/60/90/120/180

The assumption of uniform outlet pressure across all clusters represents an idealized scenario where all fractures have equal conductivity. While this simplification allows isolation of wellbore transport effects, field conditions involve varying pressure drops due to geological heterogeneity and stress shadows [40].

5 Results and Analysis

5.1 Effect of Flow Rates

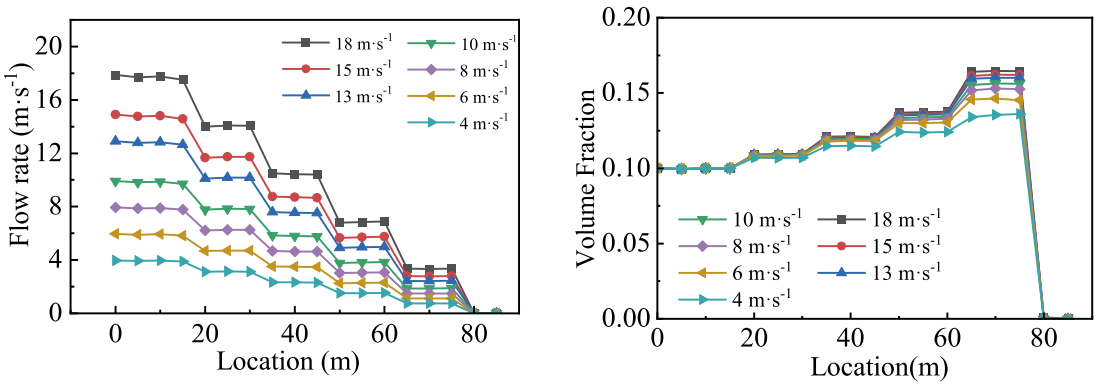
Proppant transport simulations were conducted at flow velocities ranging from 4 to 18 $m \cdot s^{-1}$, corresponding to pump rates of 3.7 to 16.5 $m^3 \cdot min^{-1}$. Fig. 5 illustrates the simulated proppant distribution in perforation clusters and the adjacent wellbore sections at the minimum (4 $m \cdot s^{-1}$) and maximum (18 $m \cdot s^{-1}$) flow velocities. At the lower flow rate, proppant settling initiates from the third perforation cluster, with a distinct proppant dune forming at the fourth cluster. In contrast, under the high-flow condition, the first three clusters remain essentially free of settling, while the fourth cluster shows a notable increase in proppant volume fraction.



(a) Flow rate at 4 $m \cdot s^{-1}$ (b) Flow rate at 18 $m \cdot s^{-1}$

Figure 5: Numerical simulation model of hydraulic fracturing.

As shown in Fig. 6a, an inverse correlation is observed between flow velocity attenuation and proppant concentration accumulation along the wellbore axis. Flow distribution through perforation clusters results in progressive velocity reduction from the initial value. While the velocity remains relatively constant within the 0–15 m interval, it decreases significantly after passing through the perforation cluster at 15 m. For instance, at an injection rate of 18 $m \cdot s^{-1}$, the average flow velocity measures 17.5 $m \cdot s^{-1}$ at the 15 m cross-section and drops to 14.0 $m \cdot s^{-1}$ at the 20 m cross-section. Similar velocity reduction patterns are observed at subsequent perforation clusters. Due to the closed end of the wellbore, the flow velocity nearly diminishes to zero at 80 m. The variation in flow velocities under different injection rates gradually decreases along the wellbore: the range of velocities reaches 13.9 $m \cdot s^{-1}$ in the front section (0–15 m), but narrows to 2.6 $m \cdot s^{-1}$ in the 65–75 m interval, indicating that the advantage of higher flow rates diminishes with increasing transport distance.



(**a**) Flow rate (**b**) Proppant Volume Fraction

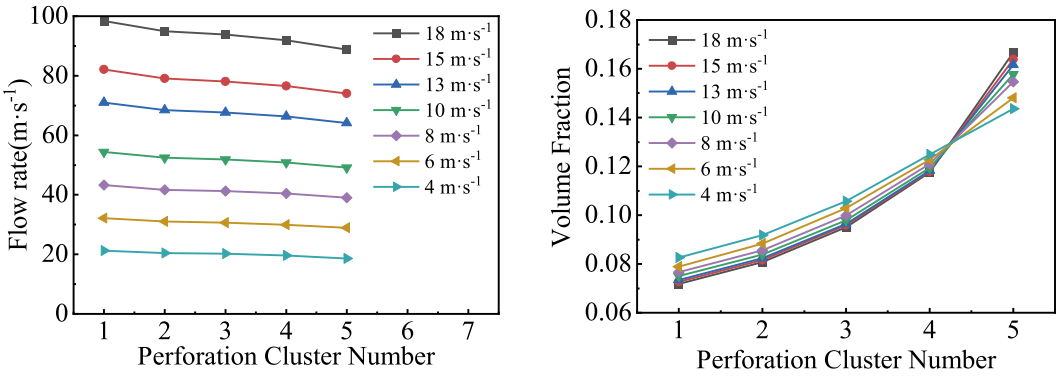
Figure 6: Average flow velocity and volumetric fraction distribution at cross-sections of different positions along the wellbore.

Fig. 6b demonstrates an inverse profile for the proppant volume fraction along the wellbore, showing a progressive increase in the axial direction. A marked rise in proppant concentration is observed immediately downstream of each perforation cluster. This phenomenon stems from the inertial disparity between the solid and liquid phases during transport: the fracturing fluid is more readily diverted into the perforations, while a considerable portion of proppant continues to be carried along the wellbore, leading to a notable accumulation of proppant after each cluster. For instance, at a flow rate of 18 $m \cdot s^{-1}$, the average proppant volume fraction increases by 6.5% over the wellbore segment from 0 to 75 m. With higher injection rates, the proppant concentration in the middle and later sections of the wellbore rises progressively, which contributes to improved fracture filling in the toe-side clusters.

Fig. 7a compares the average flow velocities through individual perforation clusters. Higher injection rates generally result in increased proppant velocities across all clusters. When the injection velocity rises from 15 to 18 $m \cdot s^{-1}$, the geometric constraint imposed by the wellbore-to-perforation diameter ratio leads to a difference in average perforation velocity of up to 20 $m \cdot s^{-1}$ among clusters. A gradual decrease in average velocity is observed from the heel to the toe clusters. The velocity attenuation gradient along the heel-to-toe direction is significantly influenced by the injection rate: at 4 $m \cdot s^{-1}$, the average perforation velocity decreases by 2.7 $m \cdot s^{-1}$ from heel to toe, while at 18 $m \cdot s^{-1}$, the reduction reaches 9.7 $m \cdot s^{-1}$.

Fig. 7b presents the corresponding average proppant volume fractions carried by the slurry through each cluster. Increasing the flow rate suppresses the proppant volume fraction in the heel-side clusters by enhancing axial inertial forces, while simultaneously raising the volume fraction in the toe-side cluster (Cluster 5). As solid particle trajectories are more dominated by inertia than the liquid phase, higher injection

rates cause significant accumulation of proppant at the wellbore terminus, resulting in elevated volume fractions in that region.

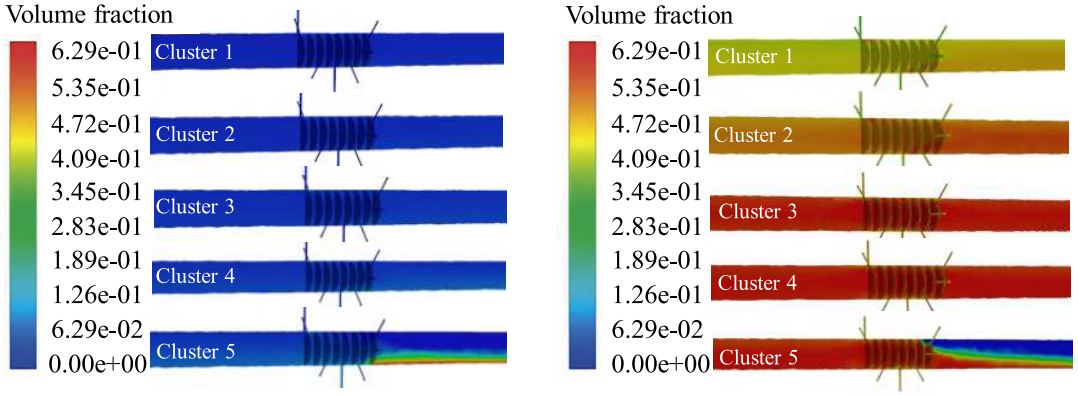


(**a**) Flow rate (**b**) Proppant Volume Fraction

Figure 7: Comparison of average flow rates and volume fractions across different perforation clusters.

5.2 Effect of Proppant Concentration

Simulations of proppant transport in the wellbore and perforations were conducted at proppant concentrations ranging from 5% to 35%. Fig. 8 shows the simulated proppant distribution at 5% and 35% concentrations. At the lower concentration (5%), no significant settling is observed along the majority of the wellbore; however, a proppant dune forms behind the fifth cluster due to the closed wellbore terminus. In contrast, at the high concentration (35%), the proppant volume fraction progressively increases from the first cluster onward. By the third cluster, the proppant volume fraction reaches approximately 60%, indicating severe accumulation that prevents normal proppant transport. It should be noted that the current model does not account for perforation erosion effects, which would dynamically alter flow distribution during field operations. The constant perforation diameter represents an initial condition before erosion begins.



(a) 5% Proppant Concentration (b) 40% Proppant Concentration

Figure 8: Display of proppant volume fraction in the wellbore at different proppant concentration.

As shown in Fig. 9a, the increase in proppant concentration leads to a slight reduction in the average proppant velocity within the wellbore due to enhanced energy dissipation from intensified inter-particle collisions and friction. Fig. 9b illustrates that higher proppant concentrations result in a proportional increase in the total injected proppant mass, thereby raising the proppant volume fraction in the wellbore.

However, at elevated concentrations (e.g., 35%), the proppant volume fraction approaches the natural packing threshold—quantified in our simulations at approximately 60%—posing a significant risk of screen-out.

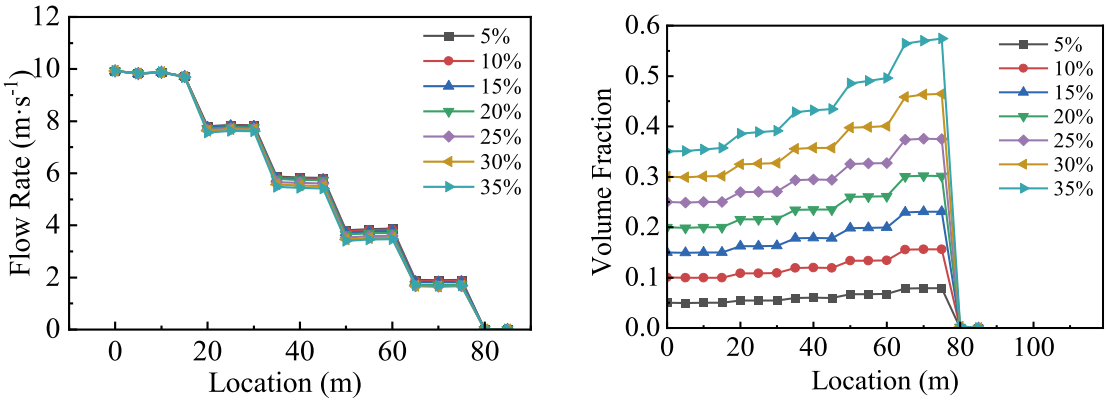


Figure 9: Distribution of average flow rate and proppant volume fraction across wellbore cross-sections under varying proppant concentrations.

As shown in Fig. 10a, proppant concentration exerts a significant influence on the heterogeneity of flow velocity and proppant distribution among perforation clusters. At a low concentration (5%), the flow velocity attenuates gradually along the wellbore with a relatively uniform distribution of proppant volume fraction. In contrast, under high concentration conditions (35%), the velocity disparity between heel and toe clusters intensifies, showing a range of 23%. Fig. 10b illustrates that the effect of increasing proppant concentration on the proppant volume fraction in perforation clusters exhibits phased nonlinear accumulation characteristics. When the concentration increases from 5% to 20%, the toe-side clusters demonstrate a notably higher growth rate in volume fraction compared to the heel-side clusters. However, as the concentration further rises to 35%, the growth rate in the toe clusters decelerates and stabilizes near the threshold value of 0.45.

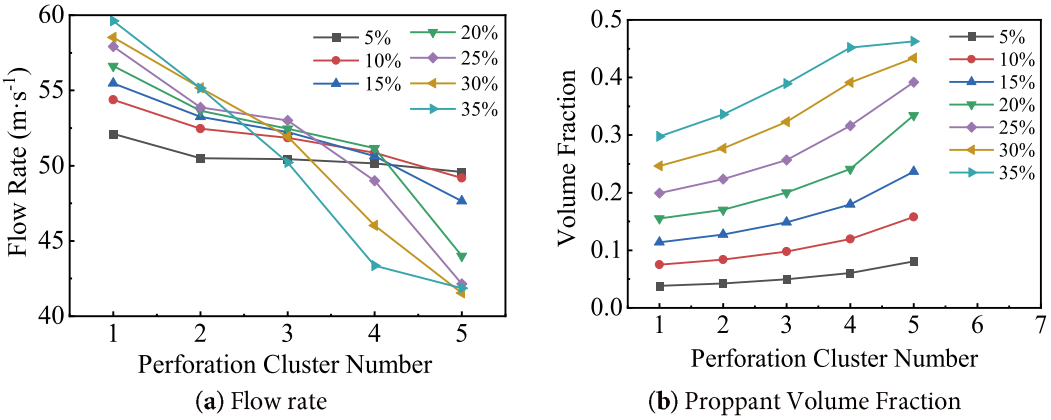


Figure 10: Comparison of average flow velocity and proppant volume fraction in different perforation clusters under varying proppant concentrations.

This nonlinear response signifies a transition in the dominant transport mechanism from inertia-dominated to concentration-gradient-driven flow. The flow separation effects and abrupt changes in the

Stokes number within the inter-cluster transition zones lead to non-monotonic settling behavior immediately downstream of perforations. An increase in fluid viscosity delays this transition by enhancing particle suspension, whereas larger proppant sizes accelerate the process due to more rapid settling.

5.3 Effect of Fluid Viscosity

Proppant transport simulations in the wellbore and perforations were conducted with fluid viscosities ranging from 1 to 30 mPa·s. The viscosity of the fracturing fluid plays a decisive role in controlling the proppant transport behavior within the wellbore-perforation system. Fig. 11 shows the simulation results at 1 and 30 mPa·s. Slickwater, commonly used in unconventional reservoir fracturing, has relatively low viscosity and limited proppant-carrying capacity. As observed in the results, when using low-viscosity fluid, significant proppant settling begins in the wellbore near the third and fourth clusters, with a clear proppant dune formed around the fifth cluster. This pattern suggests a potential risk of screen-out in the downstream perforations. In contrast, with high-viscosity fracturing fluid, proppant settling in the wellbore is minimal, indicating that most proppant enters the perforations. However, given the common use of low-viscosity slickwater due to cost efficiency and reduced formation damage, other operational parameters should be optimized to mitigate proppant settling in the wellbore. The assumption of Newtonian fluid behavior with constant viscosity provides a fundamental understanding but simplifies the shear-thinning characteristics of typical slickwater fluids. Future work could incorporate more complex rheological models.

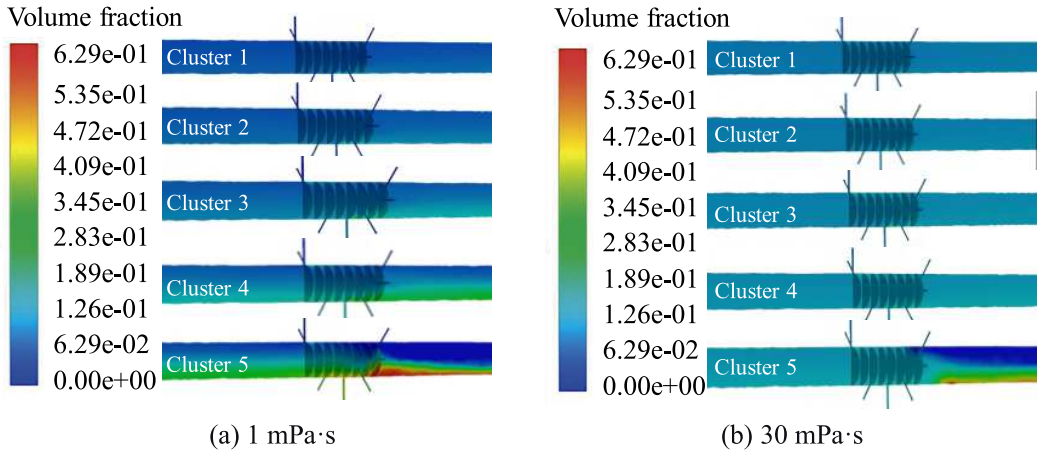
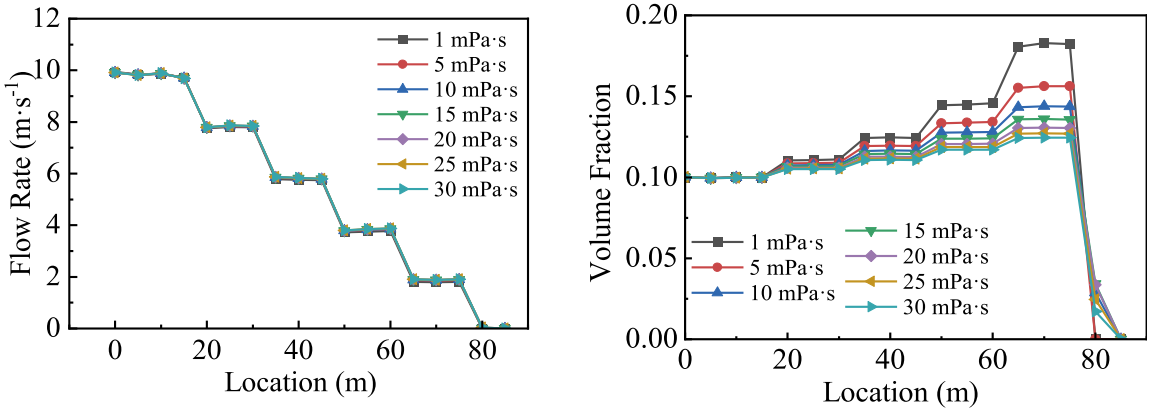


Figure 11: Display of proppant volume fraction in the wellbore at different fluid viscosities.

As shown in Fig. 12a, the flow distribution through perforation clusters results in a linear attenuation of flow velocity along the wellbore (with velocities of approximately 10, 8, 6, 4 and 2 m/s upstream of Clusters 1–5, respectively, decreasing by about 2 m/s per cluster). Changes in fluid viscosity have minimal influence on this wellbore velocity profile. Fig. 12b illustrates that reducing the fracturing fluid viscosity significantly exacerbates heterogeneity in proppant settling by weakening the viscous carrying capacity. When viscosity decreases from 30 to 25 mPa·s, the proppant volume fraction near the distal Cluster 5 decreases from 0.127 to 0.124. In contrast, a reduction from 5 to 1 mPa·s causes a more pronounced drop in the proppant volume fraction at Cluster 5, from 0.182 to 0.156. This indicates the presence of a critical threshold in the low-viscosity regime (<10 mPa·s), beyond which the effect of viscosity becomes significantly enhanced. The underlying mechanism stems from the competition between viscous forces and particle inertial forces. At high viscosity (>20 mPa·s), viscous forces dominate the proppant-carrying process and particle transport is homogenized by fluid drag, leading to gradual changes in volume fraction. At low viscosity (<10 mPa·s), however, the sharp

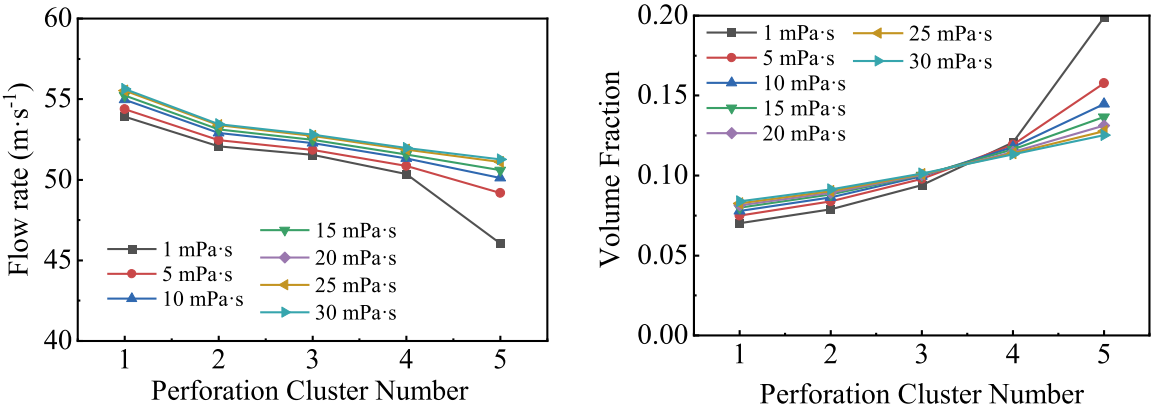
decline in viscous forces allows particle inertia to become prominent. Under such conditions, proppant tends to deviate from the liquid transport path prematurely due to the combined effects of gravitational settling and perforation-induced flow division, resulting in a sharp decrease in the proppant volume fraction entering the distal clusters. This indicates the presence of a critical threshold in the low-viscosity regime (identified as <10 mPa·s in our analysis), beyond which the effect of viscosity becomes significantly enhanced.



(**a**) Flow rate (**b**) Proppant Volume Fraction

Figure 12: Distribution of average flow rate and proppant volume fraction across wellbore cross-sections under different fracturing fluid viscosities.

Fig. 13a shows that reduced fluid viscosity significantly alters proppant transport in the wellbore-perforation system. Along the heel-to-toe direction, perforation cluster velocities decrease progressively. Under low viscosity (1 mPa·s), proppant accumulation at the distal cluster amplifies velocity attenuation by 3.7 times compared to upstream regions. As shown in Fig. 13b, at 1 mPa·s viscosity, proppant volume fractions in Clusters 1–3 are 89% of those at 30 mPa·s, while Cluster 5 exhibits over 133% due to inertial and gravitational effects. To improve proppant distribution uniformity in slickwater fracturing, non-uniform perforation designs or dynamic flow rate control can be applied.



(**a**) Flow rate (**b**) Proppant Volume Fraction

Figure 13: Comparison of average flow rate and proppant volume fraction in perforation clusters under different fracturing fluid viscosities.

5.4 Effect of Proppant Size

This study conducted numerical simulations on the transport and settlement of six proppant sizes: 20/40, 30/50, 40/70, 70/140, 200 and 300 mesh. As shown in Fig. 14, the 20/40-mesh proppant system begins to settle at the fourth perforation cluster, showing a clear gradient in proppant volume fraction along the wellbore. Downstream of the fifth cluster, a flow separation zone forms due to diminished fluid kinetic energy, leading to significant proppant accumulation and the development of a typical three-dimensional deposition structure. In contrast, the 300-mesh fine proppant system exhibits excellent suspension characteristics, with a relatively uniform distribution in the wellbore and no noticeable deposition zone even near the closed wellbore end.

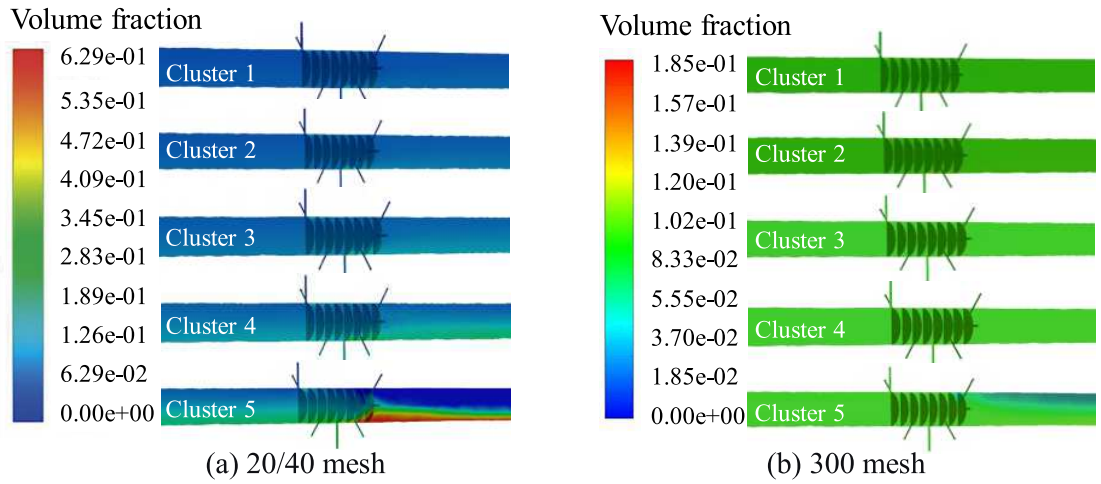
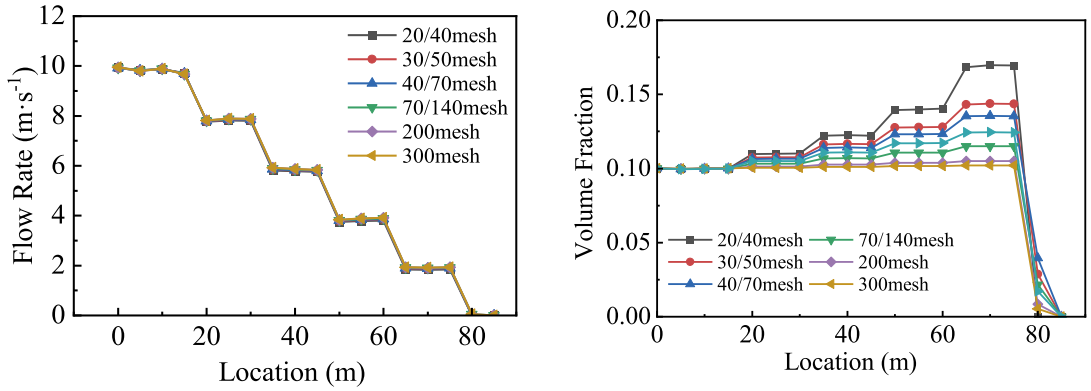


Figure 14: Proppant volume fraction distribution in the wellbore under varying particle size conditions.

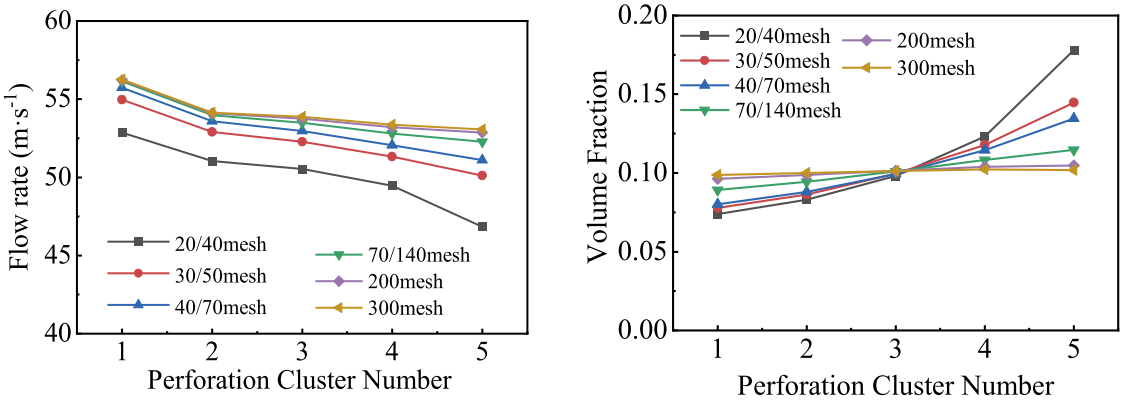
As shown in Fig. 15a, the flow velocity in the wellbore shows minimal variation across different proppant sizes but gradually decreases along the axial direction, with a more pronounced reduction observed after passing through each perforation cluster. Fig. 15b illustrates a significant accumulation of proppant volume fraction along the wellbore. Due to the continuous attenuation of fluid kinetic energy, the proppant volume fraction increases progressively from 10% at the inlet to 17.2% in the end region (taking 20/40 mesh proppant as an example). The influence of particle size on transport behavior is particularly notable. The 300-mesh fine proppant system exhibits a much smaller variation in volume fraction along the wellbore, with a range of only 2.4% (increasing from 10% at the inlet to 12.4% at the end), which is 65.7% lower than the 7.2% range observed for the 20/40 mesh coarse proppant. The superior suspension characteristics of the fine proppant significantly enhance the proppant entry efficiency into the perforation clusters. In contrast, for coarse proppant systems, when the local flow velocity near the toe-side clusters drops below the critical settling velocity, phase separation intensifies sharply, leading to a marked increase in proppant volume fraction. This imbalance in proppant concentration gradient in the toe-side fractures can reduce fracture conductivity and, in severe cases, cause perforation plugging and increased treating pressure. Therefore, for coarse proppant systems, it is necessary to optimize perforation cluster spacing or adopt variable-rate injection strategies to elevate local flow velocities, suppress particle settling and ensure uniform proppant placement.



(**a**) Flow rate (**b**) Proppant Volume Fraction

Figure 15: Distribution of average flow rate and proppant volume fraction across wellbore cross-sections under different particle sizes.

Fig. 16a shows that although proppant particles of different sizes exhibit similar transport velocities in the main wellbore flow, their velocities through perforations differ significantly due to hydrodynamic constraints imposed by the perforation geometry. When the particle-to-perforation diameter ratio (d/D) exceeds 0.25 (as in the 20/40 mesh system), flow field distortion near the perforation edges causes substantial local velocity attenuation, creating a kinetic energy barrier upstream of the perforation clusters and resulting in lower proppant velocities through the perforations. In contrast, the 300-mesh fine particle system (d/D = 0.08), with its lower Stokes number, demonstrates excellent flow-following behavior in the perforation region and achieves higher proppant velocities. As the particle size decreases from 20/40 to 300 mesh, the average proppant velocity through the fifth cluster increases from 46.8 to 53.1 m·s^{-1}, an increase of 13.5%.



(**a**) Flow rate (**b**) Proppant Volume Fraction

Figure 16: Comparison of average flow velocity and proppant volume fraction in perforation clusters under different particle sizes.

Fig. 16b indicates that smaller proppant particles exhibit superior transport performance in the proximal clusters. The slurry volume fraction for 300-mesh proppant reaches 10.1%, which is 36.5% higher than the 7.4% observed for the 20/40 mesh system. This is attributed to the lower settling velocity of fine particles, which matches well with the high axial flow velocity in the wellbore, effectively prolonging suspension and allowing more particles to be carried into the front clusters with the fluid. In the distal section of the

wellbore, the attenuation of fluid kinetic energy triggers a concentration accumulation effect for coarse proppant. Despite the reduced flow velocity in this region, the higher settling rate of large particles leads to a significant concentration gradient near the fifth cluster, where the slurry volume fraction surges to 0.18—a 141% increase compared to the proximal region. Simulation results reveal that when the local concentration exceeds a critical packing threshold, enhanced inter-particle interactions enable coarse proppant to continue entering perforations even under low flow velocities, with its volume fraction increasing to 8.9%. This phenomenon suggests that in flow-restricted regions, concentration gradient-driven transport gradually supersedes inertial effects as the dominant particle transport mechanism. Consequently, fracture network modeling must strengthen the quantitative description of diffusive-convective coupling, particularly in the transition zone between the high-shear near-wellbore region and the low-velocity far-field region, potentially by introducing a concentration boundary layer model to correct the traditional homogeneous flow assumption.

5.5 Effect of Perforation Phase Angle

By establishing numerical models with multiple perforation phase angles, the influence of perforation spatial configuration on proppant transport behavior was investigated. As shown in Fig. 17, five phase angle configurations were implemented along the wellbore circumference: 45°, 60°, 90°, 120° and 180°, corresponding to 8, 6, 4, 3 and 2 perforations per cluster, respectively.

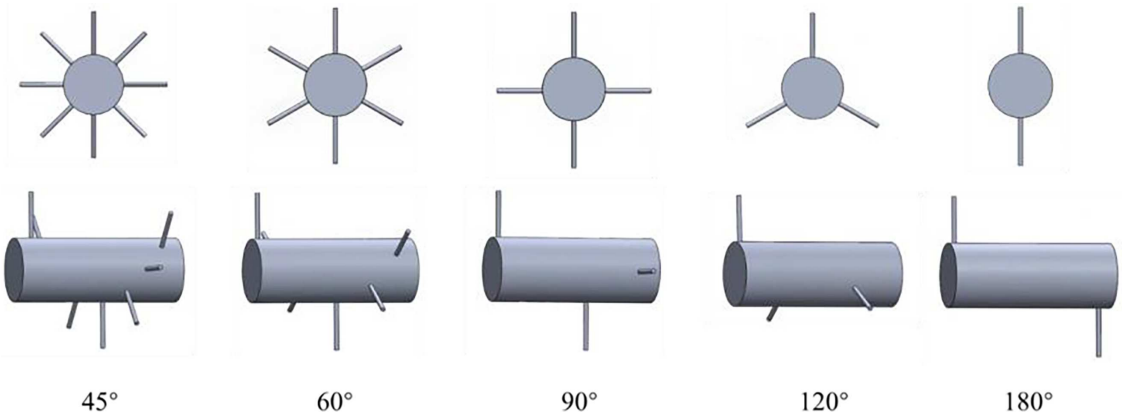


Figure 17: The perforation cluster section in numerical models with different phase angles.

Fig. 18 compares the proppant flow velocities along the wellbore under different perforation phase angles. The variation in phase angle significantly alters the flow structure within the wellbore cross-section. At a 180° phase angle (with two perforations at top and bottom), the proppant volume fraction in the wellbore remains relatively high. An excessive number of perforations may reduce the flow rate per perforation, thereby weakening proppant conveyance capacity, promoting deposition in the wellbore and decreasing effective proppant entry. Therefore, the perforation phase angle considerably influences proppant transport into fractures. While too few perforations hinder proppant entry, an excessive number is not always advantageous, as it may promote the initiation of multiple shorter fractures due to flow division.

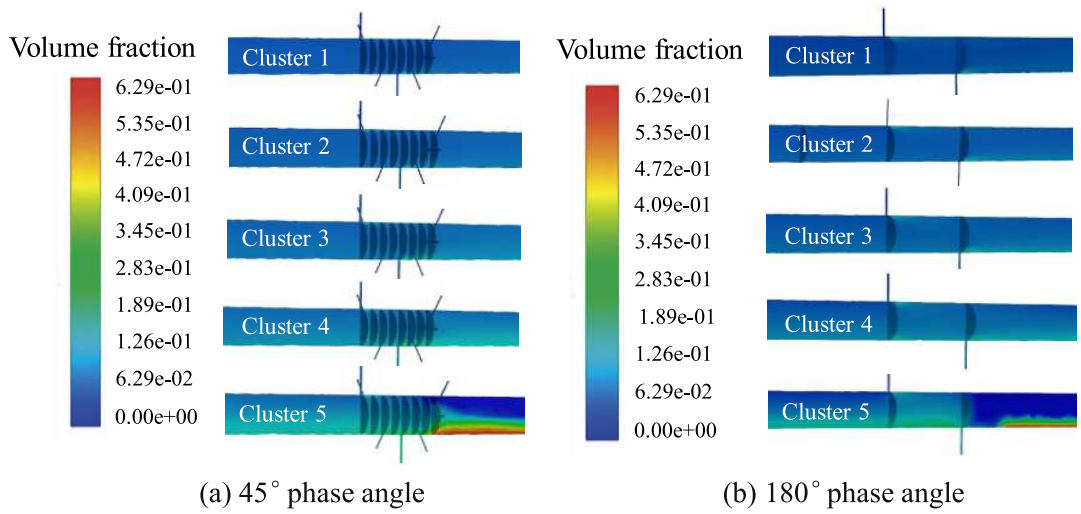


Figure 18: Display of proppant volume fraction in the wellbore under varying phase angles.

Fig. 19a compares the proppant transport velocities along the wellbore under different phase angles. As the perforation phase angle increases, the proppant transport velocity shows minimal variation along the wellbore axis. Fig. 19b illustrates the corresponding proppant volume fractions along the wellbore. Increasing the phase angle leads to a systematic decrease in the average proppant volume fraction within the wellbore. Specifically, in the far-wellbore region (60–80 m), the volume fraction at 180° phase angle decreases by 15.4% compared to the 45° configuration. Larger phase angles correspond to sparser perforation distributions, which enhance the flow rate per perforation, effectively suppressing proppant settling and retention in the wellbore, thereby increasing the amount of proppant transported through the perforations.

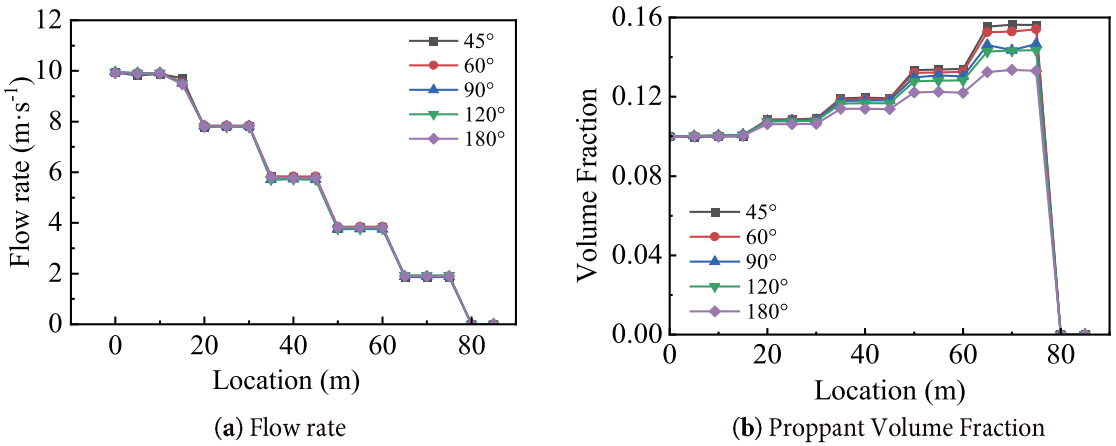
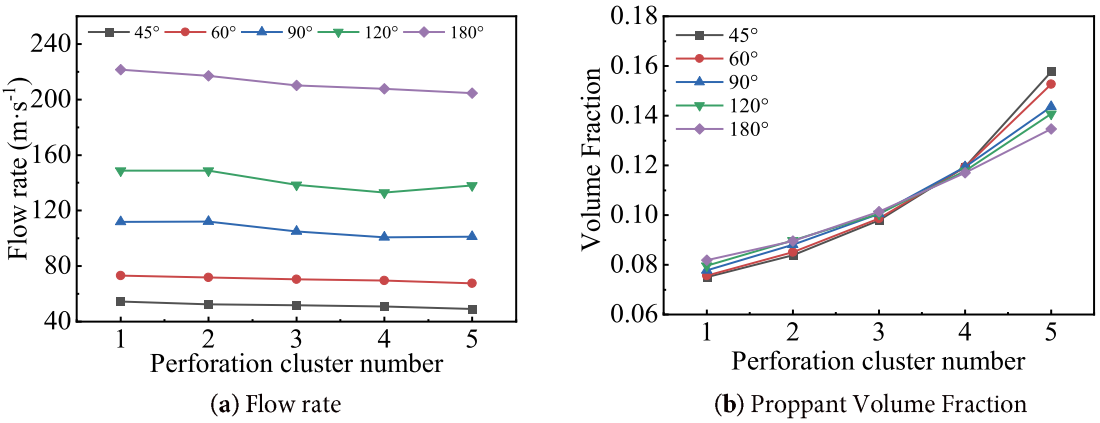


Figure 19: Distribution of average flow rate and proppant volume fraction across wellbore cross-sections under different phase angles.

Fig. 20a shows the average proppant velocity through different perforation clusters. The average velocity increases with larger phase angles due to fewer perforations per cluster. When the phase angle decreases from 180° to 45°, the average proppant velocity in the first cluster increases from 49.2 to 54.4 $m \cdot s^{-1}$, representing a 10.6% increase. Fig. 20b illustrates the average proppant volume fraction through different clusters. For the first three clusters, smaller phase angles result in lower volume fractions, while the opposite pattern appears

in Clusters 4 and 5. With smaller phase angles, the increased number and density of perforations—especially in the lower part of the wellbore—lead to higher proppant entry. When the phase angle decreases from 180° to 45°, the average proppant volume fraction in Cluster 5 drops from 0.13 to 0.08, a reduction of 38.5%.



(**a**) Flow rate (**b**) Proppant Volume Fraction

Figure 20: Comparison of average flow velocity and proppant volume fraction in perforation clusters under different phase angles.

6 Discussion

While this study employed controlled conditions to isolate fundamental transport mechanisms, the findings provide critical insights for field operations. The identified optimal parameters (e.g., 45° phase angle, viscosity thresholds) establish baseline design strategies. In field applications, tool eccentricity would likely amplify the bottom-side accumulation bias observed in our concentric model. Perforation erosion, though not modeled here, would dynamically enlarge openings and alter flow distribution, potentially mitigating but not eliminating the inherent toe-ward accumulation tendency. Most importantly, variable perforation pressure due to geological heterogeneity would interact with the wellbore transport effects quantified herein—the inherent distribution unevenness provides a baseline understanding that field engineers must account for even before reservoir heterogeneity is considered. Real-time pressure monitoring and adaptive pumping strategies can leverage these findings to optimize proppant placement despite field deviations.

The strong size-dependent behavior observed between coarse (20/40) and fine (300-mesh) proppants has direct implications for designing hybrid injection schedules. Our results demonstrate that finer proppants achieve superior distribution uniformity due to enhanced suspension capabilities, while coarser proppants tend to accumulate in toe-side clusters. This supports the field practice of 'tail-in' stages where coarse proppant is injected last to maximize near-wellbore conductivity in the dominant fractures. The sequential injection of finer proppants initially could help achieve better cluster coverage by penetrating further into fracture networks, while subsequent coarser proppant would provide optimal conductivity in primary fractures. However, mixed-size injection presents complex interactions—finer particles may alter the transport dynamics of coarser ones by modifying slurry viscosity and settling behavior. Future work should specifically investigate these temporal sequencing effects to optimize hybrid schedules.

The findings of this study provide immediate practical value for designing more efficient hydraulic fracturing operations. The identified optimal parameters—such as the 45° phase angle configuration for improved circumferential distribution, viscosity thresholds for effective proppant transport, and flow rate guidelines for balancing axial transport and toe-side accumulation—offer direct guidance for field engineers designing perforation schemes and pumping schedules. The quantitative relationships between operational

parameters and distribution uniformity enable more predictable proppant placement outcomes, potentially reducing screen-out risks and improving stimulation effectiveness in multi-cluster horizontal wells.

7 Conclusion

This study established a full-scale 90-m horizontal wellbore CFD model with multiple perforation clusters to systematically simulate proppant transport and placement. The coupled effects of flow rate, proppant concentration, fluid viscosity, proppant size and phase angle on proppant distribution were investigated. The main conclusions are as follows:

(1) Injection rate dominates proppant axial transport and distribution pattern. Higher rates enhance particle inertial transport but intensify proppant accumulation in toe-side clusters due to sustained axial momentum, resulting in uneven distribution along the wellbore.

(2) Fluid viscosity critically controls proppant suspension and entry efficiency. High-viscosity fluids significantly improve proppant carrying capacity and distal cluster entry, while low-viscosity slickwater exacerbates insufficient proppant delivery to the toe region due to weakened viscous forces.

(3) Proppant concentration and size jointly govern settling behavior and transport limits. High concentrations (>20%) increase total proppant delivery but risk screen-out as concentrations approach the packing threshold. Finer proppants (e.g., 300-mesh) exhibit superior suspension and uniformity, while coarser grades suffer from significant settling and toe-side concentration polarization.

(4) Perforation phase angle substantially affects circumferential distribution uniformity. The 45° spiral configuration effectively mitigates bottom-side entry bias and improves circumferential distribution, while larger phase angles enhance velocity per perforation but may compromise cluster coverage uniformity.

The findings provide fundamental insights into the competition between inertial, viscousand gravitational forces during proppant placement. This study offers a validated numerical framework for optimizing perforation design and pumping parameters to achieve more uniform reservoir stimulation.

Acknowledgement: Thank you to Shale Gas E&D Project Department, CNPC Chuanqing Drilling Engineering Co., Ltd. and China University of Petroleum (East China) Deep Oil and Gas Ministry of Education Key Laboratory for this work support.

Funding Statement: This research was financially supported by the authors would like to acknowledge the Fundamental Research Funds for the Central Universities (Grant No. 24CX05001A) and the financial support of the National Natural Science Foundation of China (Grant No. 52474069).

Author Contributions: The authors confirm their contributions to the paper as follows: Study conception and design: Yixuan Wang, Yanchao Li, Qiang Feng; Data collection: Haicheng Sun, Guchang Zhang; Analysis and interpretation of results: Zhiming Zhao, Jianfeng Xiao; Draft manuscript preparation: Jingyun Huang, Tiankui Guo. All authors reviewed and approved the final version of the manuscript.

Availability of Data and Materials: The datasets generated and analyzed during the current study are available from the corresponding author upon reasonable request.

Ethics Approval: Not applicable.

Conflicts of Interest: The authors declare no conflicts of interest.

References

1. Lecampion B, Bunger A, Zhang X. Numerical methods for hydraulic fracture propagation: a review of recent trends. J Nat Gas Sci Eng. 2018;49:66–83. doi:10.1016/j.jngse.2017.10.012.
2. Jaripatke OA, Barman I, Ndungu JG, Schein GW, Flumerfelt RW, Burnett N, et al. Review of Permian completion designs and results. In: Proceedings of the SPE Annual Technical Conference and Exhibition; 2018 Sep 24–26. Dallas, TX, USA. doi:10.2118/191560-ms.
3. Liu X, Qu Z, Guo T, Sun Y, Rabiei M, Liao H. A coupled thermo-hydrologic-mechanical (THM) model to study the impact of hydrate phase transition on reservoir damage. Energy. 2021;216:119222. doi:10.1016/j.energy.2020.119222.
4. Zhang G, Wang B, Guo T, Zhou F. The characteristics of hydraulic fracture morphology in glutenite reservoirs: an experimental investigation. Theor Appl Fract Mech. 2024;134:104685. doi:10.1016/j.tafmec.2024.104685.
5. Xu H, Jiang H, Wang J, Wang T, Zhang L. Simulation of fracture propagation law in fractured shale gas reservoirs under temporary plugging and diversion fracturing. Phys Fluids. 2023;35:63309. doi:10.1063/5.0151148.
6. Wang B, Zhang G, Sun Z, Liu J, Ma Y, Zhou F. Plugging characteristics of self-degradable diverters within three-dimensional hydro-fractures: an experimental investigation. Phys Fluids. 2023;35(9):093311. doi:10.1063/5.0168463.
7. Zhou H, Yan T, Ma C, Wang B, Zhou F. Characteristics of propped fracture propagation in volcanic clastic reservoirs: a multiscale study of conductivity sustainability and fracture network complexity. Rock Mech Rock Eng. 2025;58(11):12551–76. doi:10.1007/s00603-025-04742-y.
8. Dontsov EV, Peirce AP. Slurry flow, gravitational settling and a proppant transport model for hydraulic fractures. J Fluid Mech. 2014;760:567–90. doi:10.1017/jfm.2014.606.
9. Zhang G, Guo T, Chen M, Qu Z. Investigation of hydraulic fracture initiation and propagation behavior in glutenite reservoir using an improved global cohesive zone model. Comput Geotech. 2025;186:107421. doi:10.1016/j.compgeo.2025.107421.
10. Qu Z, Wang J, Guo T, Shen L, Liao H, Liu X, et al. Optimization on fracturing fluid flowback model after hydraulic fracturing in oil well. J Petrol Sci Eng. 2021;204:108703. doi:10.1016/j.petrol.2021.108703.
11. Liu B, Kumar D, Ghassemi A. Modeling proppant transport and settlement in 3D fracture networks in geothermal reservoirs. Geothermics. 2025;125:103176. doi:10.1016/j.geothermics.2024.103176.
12. Liu B, Ghassemi A. Simulation of proppant placement in multiple simultaneously propagating hydraulic fractures in horizontal wells. Rock Mech Rock Eng. 2024;57(11):9635–50. doi:10.1007/s00603-024-04022-1.
13. Xue L, Guo T, Chen M, Zhang B, Hu Z, Zhang Y, et al. Fracture propagation law of multi-well hydraulic fracturing in conglomerate reservoir: a laboratory study. Phys Fluids. 2025;37(8):087153. doi:10.1063/5.0280525.
14. Dontsov EV. A model for proppant dynamics in a perforated wellbore. Int J Multiph Flow. 2023;167:104552. doi:10.1016/j.ijmultiphaseflow.2023.104552.
15. Shah SN, Lord DL. Hydraulic fracturing slurry transport in horizontal pipes. SPE Drill Eng. 1990;5(3):225–32. doi:10.2118/18994-pa.
16. Arnipally SK, Hirpa MM, Bizhani M, Kuru E. Effect of particle size on the near wall turbulence characteristics and the critical velocity required for the particle removal from the sand bed deposited in horizontal pipelines. In: Proceedings of the 11th North American Conference on Multiphase Production Technology; 2018 Jun 6–8; Banff, AL, Canada.
17. Xing J, Wang F, Zhang Q, Hong G, Talman AM. Experimental research on critical velocity of slurry pipeline transportation. In: Proceedings of the 31st International Ocean and Polar Engineering Conference; 2021 Jun 20–25; Rhodes, Greece.
18. Ngameni KL, Miskimins JL, Abass HH, Cherrian B. Experimental study of proppant transport in horizontal wellbore using fresh water. In: Proceedings of the SPE Hydraulic Fracturing Technology Conference and Exhibition; 2017 Jan 24–26; The Woodlands, TX, USA. doi:10.2118/184841-ms.
19. Ahmad FA, Miskimins JL. Proppant transport and behavior in horizontal wellbores using low viscosity fluids. In: Proceedings of the SPE Hydraulic Fracturing Technology Conference and Exhibition; 2019 Feb 5–7; The Woodlands, TX, USA. doi:10.2118/194379-ms.

20. Sinkov K, Weng X, Kresse O. Modeling of proppant distribution during fracturing of multiple perforation clusters in horizontal wells. In: Proceedings of the SPE Hydraulic Fracturing Technology Conference and Exhibition; 2021 May 4–6; Virtual. doi:10.2118/204207-ms.
21. Aijaz MJ, Sharma MM. Effect of proppant settling in the wellbore on proppant distribution in perforation clusters. In: Proceedings of the SPE Hydraulic Fracturing Technology Conference and Exhibition; 2023 Jan 31–Feb 2; The Woodlands, TX, USA. doi:10.2118/212351-ms.
22. Ugueto CGA, Huckabee PT, Molenaar MM, Wyker B, Somanchi K. Perforation cluster efficiency of cemented plug and perf limited entry completions; insights from fiber optics diagnostics. In: Proceedings of the SPE Hydraulic Fracturing Technology Conference; 2016 Feb 9–11; The Woodlands, TX, USA. doi:10.2118/179124-ms.
23. Crespo F, Aven NK, Cortez J, Soliman MY, Bokane A, Jain S, et al. Proppant distribution in multistage hydraulic fractured wells: a large-scale inside-casing investigation. In: Proceedings of the SPE Hydraulic Fracturing Technology Conference; 2013 Feb 4–6; The Woodlands, TX, USA. doi:10.2118/163856-ms.
24. Zhang T, Li C, Shi Y, Mu K, Wu C, Guo J, et al. Numerical simulation of proppant directly entering complex fractures in shale gas. J Nat Gas Sci Eng. 2022;107:104792. doi:10.1016/j.jngse.2022.104792.
25. Ahmad FA, Miskimins JL. New experimental correlations to predict proppant distribution between perforation clusters using low viscosity fluids in a horizontal wellbore. In: Proceedings of the SPE Annual Technical Conference and Exhibition; 2020 Oct 26–29; Virtual. doi:10.2118/201452-ms.
26. Zhang M, Wu CH, Sharma M. Proppant placement in perforation clusters in deviated wellbores. In: Proceedings of the 7th Unconventional Resources Technology Conference; 2019 Jul 22–24; Denver, CO, USA. doi:10.15530/urtec-2019-298.
27. Li X, Rui Z, Deng C, Xu M, Cao W, Liu M, et al. An experimental study on the proppant transport in a horizontal wellbore considering perforation erosion in clean water fracturing. In: Proceedings of the APOGCE 2024; 2024 Oct 15–17; Perth, Australia. doi:10.2118/221316-ms.
28. Bahri A, Miskimins JL, Alajmei S. Achieving uniform proppant distribution in horizontal wellbore clusters using computational fluid dynamics modeling. SPE J. 2025;30(11):6698–714. doi:10.2118/223571-pa.
29. Liu X, Wang J, Singh A, Rijken M, Chrusch L, Wehunt D, et al. Achieving perfect fluid and proppant placement in multi-stage fractured horizontal wells: a CFD modeling approach. In: Proceedings of the SPE Hydraulic Fracturing Technology Conference and Exhibition; 2021 May 4–6; Virtual. doi:10.2118/204182-ms.
30. Sahai RR, Miskimins JL, Olson KE. Laboratory results of proppant transport in complex fracture systems. In: Proceedings of the SPE Hydraulic Fracturing Technology Conference; 2014 Feb 4–6; The Woodlands, TX, USA. doi:10.2118/168579-ms.
31. Zawawi MH, Saleha A, Salwa A, Hassan NH, Zahari NM, Ramli MZ, et al. A review: fundamentals of computational fluid dynamics (CFD). AIP Conf Proc. 2018;2030:20252. doi:10.1063/1.5066893.
32. Zhou J, Yan D, Yao M, Wu L, Mo D, Wang W, et al. Effect of flexible fibers for preventing proppant flowback after fracture closure by CFD-DEM method. Geoenergy Sci Eng. 2025;247:213719. doi:10.1016/j.geoen.2025.213719.
33. Lv M, Guo T, Chen M, Liu Y, Yang X, Dai C, et al. Simulation research of proppant flowback and control method after hydraulic fracturing based on CFD-DEM. Powder Technol. 2025;457:120913. doi:10.1016/j.powtec.2025.120913.
34. Yang H, Li K, Liao Z, Li X, Rabiee H, Ren S, et al. Proppant transport in secondary Sand fracturing using Eulerian-Eulerian multiphase model Approach. Geoenergy Sci Eng. 2024;241:213186. doi:10.1016/j.geoen.2024.213186.
35. Ali Kökpınar M, Göğüş M. Critical flow velocity in slurry transporting horizontal pipelines. J Hydraul Eng. 2001;127(9):763–71. doi:10.1061/(asce)0733-9429(2001)127:9(763).
36. El Rabaa W. Experimental study of hydraulic fracture geometry initiated from horizontal wells. In: Proceedings of the SPE Annual Technical Conference and Exhibition; 1989 Oct 8–11; San Antonio, TX, USA. doi:10.2118/19720-ms.
37. Fisher MK, Heinze JR, Harris CD, Davidson BM, Wright CA, Dunn KP. Optimizing horizontal completion techniques in the Barnett Shale using microseismic fracture mapping. In: Proceedings of the SPE Annual Technical Conference and Exhibition; 2004 Sep 26–29; Houston, TX, USA. doi:10.2118/90051-ms.

38. Soliman MY, East L, Adams D. Geomechanics aspects of multiple fracturing of horizontal and vertical wells. SPE Drill Complet. 2008;23(3):217–28. doi:10.2118/86992-pa.
39. Wang J, Singh A, Liu X, Rijken M, Tan Y, Naik S. Efficient prediction of proppant placement along a horizontal fracturing stage for perforation design optimization. SPE J. 2022;27(2):1094–108. doi:10.2118/208613-pa.
40. Ullah H, Khan I, AlSalman H, Islam S, Asif Zahoor Raja M, Shoaib M, et al. Levenberg-marquardt back-propagation for numerical treatment of micropolar flow in a porous channel with mass injection. Complexity. 2021;2021:5337589. doi:10.1155/2021/5337589.